Journal of Structural Geology 125 (2019) 235–247

Contents lists available at ScienceDirect

Journal of Structural Geology

journal homepage: www.elsevier.com/locate/jsg

Quantifying geometrically necessary dislocations in quartz using HR-EBSD: Application to chessboard subgrain boundaries

David Wallis[a,1], Andrew J. Parsons[b,*], Lars N. Hansen[a]

[a] Department of Earth Sciences, University of Oxford, Oxford, OX1 3AN, UK
[b] School of Earth & Environment, University of Leeds, Leeds, LS2 9JT, UK

ARTICLE INFO

Keywords:
HR-EBSD
Quartz
Geometrically necessary dislocations
Chessboard subgrains
Himalaya

ABSTRACT

This study presents the first use of high-angular resolution electron backscatter diffraction (HR-EBSD) to quantitatively characterise geometrically necessary dislocations in quartz subgrain structures. HR-EBSD exploits cross-correlation of diffraction patterns to measure intragranular misorientations with precision on the order of 0.01° with well-constrained misorientation axes. We investigate the dislocation structures of chessboard subgrains in quartz within samples from the Greater Himalayan Sequence, Nepal. Our results demonstrate that chessboard subgrains are formed primarily from two sets of subgrain boundaries. One set consists primarily of {*m*}[*c*] edge dislocations, the other consists primarily of dislocations with < *a* > Burgers vectors. Apparent densities of geometrically necessary dislocations vary from $> 10^{13}$ m^{-2} within some subgrain boundaries to $< 10^{12}$ m^{-2} within subgrain interiors. The results suggest that at pressures above approximately 10 kbar, chessboard subgrains may form within the α-quartz stability field. Most importantly, this study demonstrates the potential of HR-EBSD as an improved method for analysis of intragranular microstructures in quartz that are used as indicators of deformation conditions.

1. Introduction

Estimates of the temperature and pressure conditions at which rocks deform are central to both reconstruction of tectonic histories and investigation of underlying deformation processes. Deformation microstructures in quartz provide a key tool for interpreting the conditions and mechanisms of deformation of crustal rocks as quartz is common in many crustal lithologies and exhibits a wide range of characteristic microstructures. Types and morphologies of subgrain boundaries in quartz are commonly used to infer temperatures of deformation, yet identifying and distinguishing particular subgrain microstructures is typically a qualitative process (e.g., Stipp et al., 2002; Law, 2014; Wallis et al., 2014; Parsons et al., 2016a). Here, we present a new method for quantitatively characterising quartz subgrain structures through estimation of types and densities of geometrically necessary dislocations (GNDs) *via* high-angular resolution electron backscatter diffraction (HR-EBSD) analysis. This is the first documented use of HR-EBSD to quantify GNDs in quartz and serves as a proof-of-concept for the use of this technique in identifying and distinguishing optically visible deformation microstructures.

Chessboard subgrains in quartz (Kruhl, 1996) are a distinctive deformation microstructure used as an indicator of high-temperature (> 550–600 °C) deformation. In cross-polarised light, chessboard subgrains form a characteristic pattern of rectangular subgrains with variable degrees of extinction and relatively straight, orthogonal boundaries (Tubia and Cuevas, 1986; Blumenfeld et al., 1986; Okudaira et al., 1995; Kruhl, 1996). Optical studies of chessboard subgrains indicate that they occur due to the development of subgrain boundaries approximately parallel to both the prism and basal planes of the quartz lattice (referred to respectively as prismatic boundaries and basal boundaries herein) (Tubia and Cuevas, 1986; Blumenfeld et al., 1986; Okudaira et al., 1995; Kruhl, 1996). Dislocation types that can form prismatic subgrain boundaries include edge dislocations with < *a* > Burgers vectors on the basal (*c*), rhomb {*r*/*z*}, or prism {*m*} planes, and screw dislocation with < *a* > and [*c*] Burgers vectors (Trépied et al., 1980; Mainprice et al., 1986; Kruhl, 1996; Lloyd et al., 1997). Dislocation types that can form basal subgrain boundaries include edge dislocations with [*c*] Burgers vector on the prism planes, or screw dislocations with < *a* > Burgers vectors (Mainprice et al., 1986; Kruhl, 1996; Lloyd et al., 1997). However, prismatic tilt boundaries composed only of prism- < *a* > edge dislocations, and basal twist boundaries composed of screw dislocations are unlikely candidates as these do not

* Corresponding author. Now at: Geological Survey of Canada, Vancouver, British Columbia, V6B 5J3, Canada.
E-mail address: andrew.parsons@canada.ca (A.J. Parsons).
[1] Now at: Department of Earth Sciences, Utrecht University, Utrecht, 3584 CD, The Netherlands.

https://doi.org/10.1016/j.jsg.2017.12.012
Received 6 September 2017; Received in revised form 6 December 2017; Accepted 15 December 2017
Available online 18 December 2017

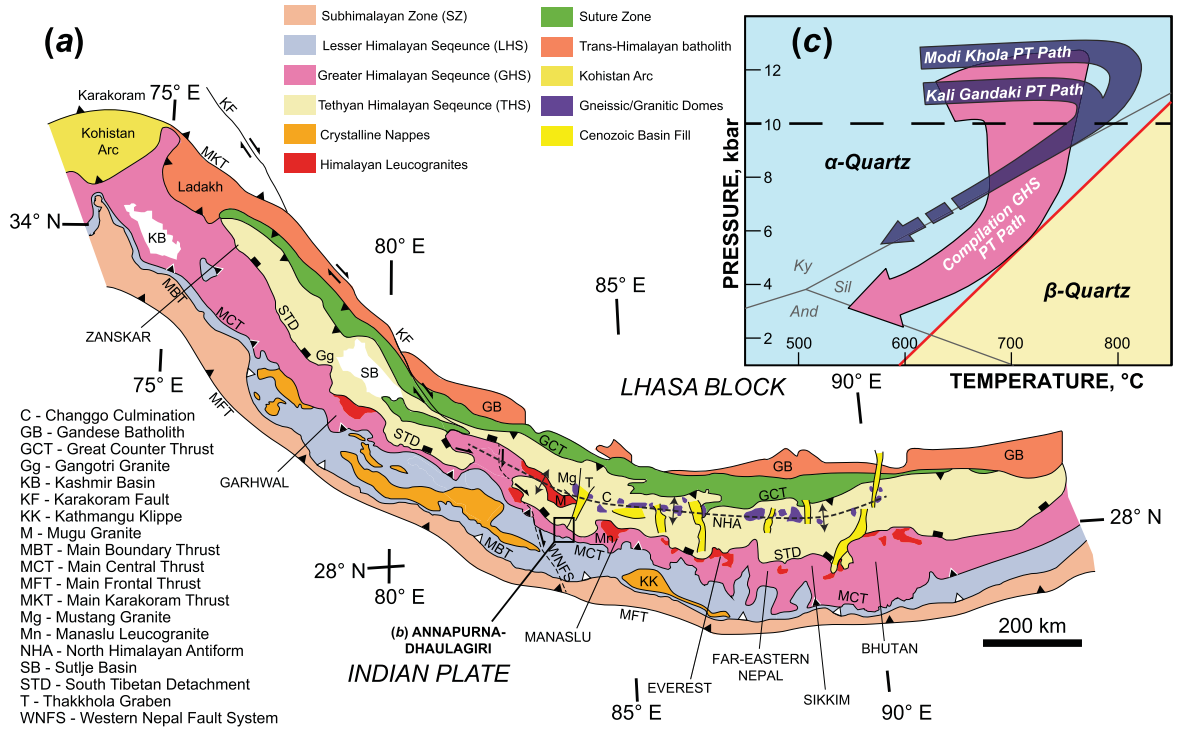

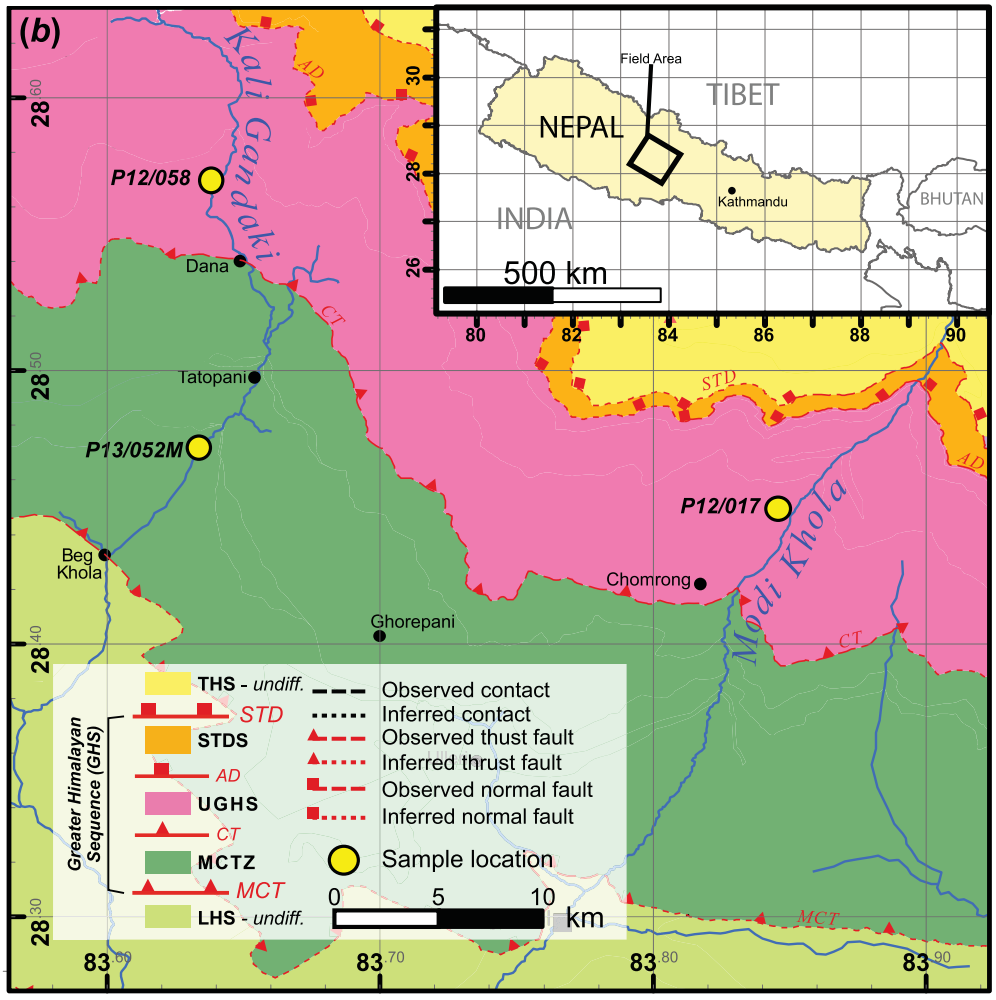

(caption on next page)

Fig. 1. Geological maps of (a) the Himalayan orogen and (b) the Annapurna-Dhaulagiri region, central Nepal, modified after Parsons et al. (2016d). Locations of samples P12/017, P12/058, and P13/052M presented in (b). (c) Pressure-temperature paths of the GHS in the Modi Khola and Kali Gandaki valleys of the Annapurna-Dhaulagiri regions (purple arrow, Iaccarino et al., 2015; Parsons et al., 2016c) and compiled from studies of the GHS in the Manaslu (Caddick, 2005) and far-eastern (Imayama et al., 2012) regions of Nepal, Sikkim (Harris et al., 2004; Mottram et al., 2015), and Bhutan (Daniel et al., 2003). Quartz stability fields drawn from Van Groos and Ter Heege (1973). Kruhl (1996) proposed that below ~10 kbar (indicated by dashed line), chessboard subgrains form within the β-quartz stability field. *Ky* – kyanite, *And* – andalusite, *Sil* – sillimanite.

produce differences in extinction when viewed in crossed-polarised light.

Prismatic subgrain boundaries are relatively common across a wide range of deformation temperatures, however, basal subgrain boundaries are found to be present only in rocks deformed at temperatures above approximately 550–600 °C (Okudaira et al., 1995; Kruhl, 1996). The development of tilt walls comprised of prism-[*c*] edge dislocations provides a simple explanation for the occurrence of basal subgrain boundaries (Mainprice et al., 1986; Kruhl, 1996; Lloyd et al., 1997). The development of chessboard subgrains is thus inferred to record activity of the prism-[*c*] slip system (Blumenfeld et al., 1986; Mainprice et al., 1986; Okudaira et al., 1995; Kruhl, 1996). Crystal preferred orientations (CPOs) indicative of prism-[*c*] slip in natural quartz are generally only observed in samples deformed at temperatures above ~650–700 °C, corroborating the suggestion that the prism-[*c*] slip system is generally only significantly activated at relatively high temperatures (Blumenfeld et al., 1986; Mainprice et al., 1986).

Although chessboard subgrains in quartz have long been recognised as an indication of relatively high temperatures of deformation (Tubia and Cuevas, 1986; Blumenfeld et al., 1986), the work of Kruhl (1996) was important in developing the idea that, at pressures below ~10 kbar, they could be used as a 'microstructural geothermobarometer' indicative of deformation in the stability field of β-quartz (Van Groos and Ter Heege, 1973) due to significant activity of the prism-[*c*] slip system made possible by its hexagonal crystal structure (Faleiros et al., 2016). Whilst the premises of this approach have been contested, as some examples of chessboard subgrains appear to have developed within the stability field of trigonal α-quartz (Okudaira et al., 1995, 1998), chessboard subgrains continue to be used as indicators of high temperatures of deformation (e.g. Ábalos et al., 2011; Little et al., 2013; Puelles et al., 2014; Long et al., 2016; Parsons et al., 2016a). However, care must be taken in identifying chessboard subgrains, as substructure with somewhat similar appearance under cross-polarised light can develop from dislocations with $< a >$ Burgers vectors only (Kruhl, 1996). Despite these widespread applications, and the possibility for misidentification, detailed investigations of the structure of chessboard subgrain boundaries, particularly those employing electron backscatter diffraction (EBSD), are relatively rare (Ábalos et al., 2011; Little et al., 2013). As such, the types of dislocations that typically form chessboard subgrain boundaries, and their relative densities, remain poorly characterised.

In this study, we develop a method for characterising intragranular substructure in quartz based on HR-EBSD (Wilkinson et al., 2006; Wilkinson and Randman, 2010; Britton and Wilkinson, 2011, 2012; Wallis et al., 2016, 2017; Boneh et al., 2017). HR-EBSD was originally developed in the materials sciences (Wilkinson et al., 2006) and has recently been applied to olivine (Wallis et al., 2016, 2017; Boneh et al., 2017; Kumamoto et al., 2017), but has not yet been applied to other major rock-forming minerals. The present study constitutes the first application of HR-EBSD to quartz, and we employ it to characterise dislocation types in chessboard subgrains in three samples from the Greater Himalayan Sequence (GHS) of the Annapurna-Dhaulagiri Himalaya, Nepal (Parsons et al., 2016b). HR-EBSD uses cross-correlation of diffraction patterns to achieve more precise measurements of intragranular misorientation angles and axes than possible using conventional EBSD based on Hough transforms of diffraction patterns (Wilkinson et al., 2006; Britton and Wilkinson, 2011, 2012). These advantages provide improved characterisation and quantification of dislocation content relative to regular EBSD (Wilkinson and Randman, 2010; Jiang et al., 2013; Wallis et al., 2016, 2017). We interpret our results with respect to the dislocation structure of chessboard subgrains and the potential for HR-EBSD as a new tool for analysing intragranular substructures in quartz.

2. The Annapurna-Dhaulagiri Himalaya

The Greater Himalayan Sequence represents the exhumed metamorphic core of the Himalayan orogen (Searle, 2015). Samples analysed in this study form part of a larger suite from the Annapurna-Dhaulagiri Himalaya of central Nepal (Fig. 1) that have been characterised in detail by Parsons et al. (2016a,c,d). Samples P12/017 and P12/058 derive from the mid-crustal section of the GHS, defined by the amphibolite facies Upper Greater Himalayan Sequence. Sample P13/052M derives from the underlying lower amphibolite to greenschist facies Main Central Thrust Zone (MCTZ) (see Parsons et al., 2016d, for definitions).

3. Sample descriptions

3.1. P12/017: micaceous quartzite, UGHS

Sample P12/017 (Fig. 2a–c) is a micaceous quartzite from the UGHS (Fig. 1). In this sample, quartz grains are anhedral with lobate grain boundaries and elliptical to equant in shape (Fig. 2a). Quartz grains have a bimodal grain size distribution and are segregated into coarse- and fine-grained bands parallel to foliation. Quartz grains preserve dynamic recrystallisation microstructures dominated by grain boundary migration (GBM) (Fig. 2a). Quartz grains from both coarse and fine grain size fractions contain subgrains, many of which appear to form chessboard subgrains 200–500 μm wide (Fig. 2a and b). Quartz CPO, measured across the sample at a 15 μm step size, is strong and approximates a 'single crystal' CPO (Fig. 2c). Distributions of [*c*]-axes and $< a >$ -axes suggest a dominance of prism- $< a >$ slip with lesser basal- $< a >$ and prism-[*c*] slip (Parsons et al., 2016a).

Quartz Grain A is in a band of coarse quartz grains which probably represents a transposed vein (Fig. 2a–b). This grain contains chessboard subgrains with boundary traces parallel to those of the basal and prism planes (Fig. 2b). These subgrain boundaries are obliquely intersected by a subordinate set of subgrain boundaries that probably represent rhomb plane-parallel subgrain boundaries (Fig. 2b). The [*c*]-axis of Quartz Grain A (Fig. 2c) is parallel to the *XZ* plane, overlapping one of weaker *c*-axis point maxima of the whole-rock CPO (Fig. 2c).

Crossed-girdle opening-angle thermometry of other locally derived samples from the same rock unit (Parsons et al., 2016a) yielded quartz deformation temperatures of 560 ± 50 °C to 655 ± 50 °C based on the thermometer of Kruhl (1998, modified by Law, 2014) and 531 ± 50 °C to 614 ± 50 °C based on the thermometer of Faleiros et al. (2016). Locally, petrology-based thermobarometry records peak metamorphic conditions of ~700–800 °C and ~10–13 kbar (Martin et al., 2010; Corrie and Kohn, 2011). Together, these constraints suggest that sample P12/017 preserves retrograde deformation from ~10–13 kbar and ~700–800 °C down to temperatures of ~500–550 °C.

3.2. P12/058: pelitic paragneiss, UGHS

Sample P12/058 (Fig. 2d–f) is a migmatitic pelitic paragneiss from the UGHS (Fig. 1). Quartz is anhedral with lobate grain boundaries and

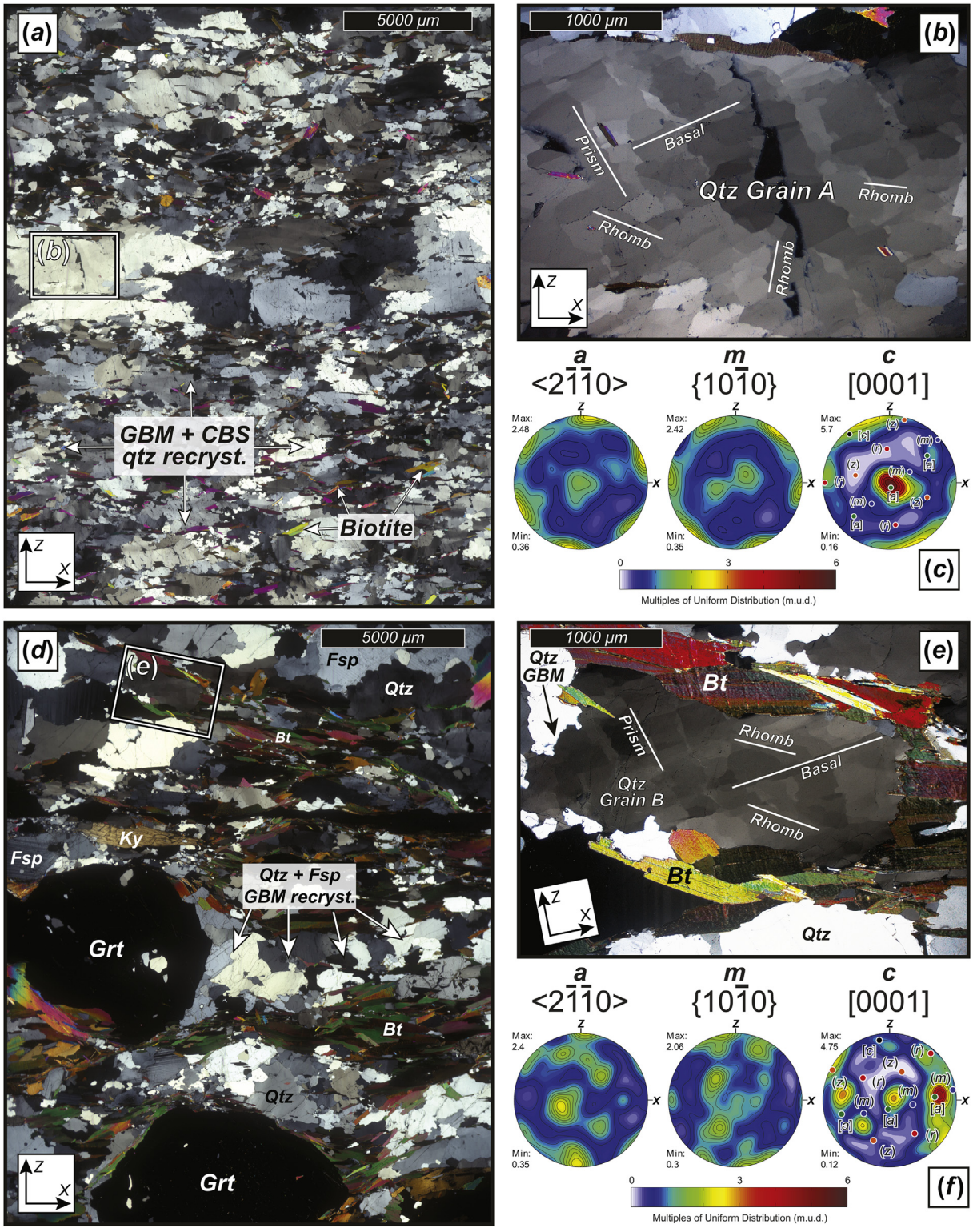

Fig. 2. Photomicrographs and quartz CPO of samples (*a-c*) P12/017, (*d-f*) P12/058, and (*g-i*) P13/052M. Sample kinematic reference frame orientations indicated in each photomicrograph (*a-b*, *d-e*, *g-h*). Whole-sample photomicrographs of (*a*) P12/017, (*d*) P12/058, and (*g*) P13/052M highlight with white boxes the locations of quartz grains analysed with HR-EBSD. Chessboard subgrain microstructures of (*b*) Quartz Grain A – P12/017, (*e*) Quartz Grain B – P12/058, and (*h*) Quartz Grain C – P13/052M are displayed with white lines showing approximate orientations of '*basal*' plane-, '*prism*' plane- and '*rhomb*' plane-parallel subgrain boundary traces. Pole figures of whole-sample quartz < *a* > , {*m*} and [*c*]-axis CPOs (c, f, i) are plotted in lower hemisphere equal area projections, in the *XZ* plane of the kinematic reference frame, contoured in multiples of uniform distribution (M.U.D.). Orientations of Quartz Grains A, B, and C are overlain on whole-sample [*c*]-axis pole figures. Coloured dots display orientations of [*c*] (black), < *a* > (green), {*m*} (blue), {*r*} (red), and {*z*} (orange) axes/directions. *Bt – biotite, CBS – chessboard subgrains, Fsp – feldspar, GBM – grain boundary migration, Grt – garnet, Msc – muscovite, Qtz – quartz.*

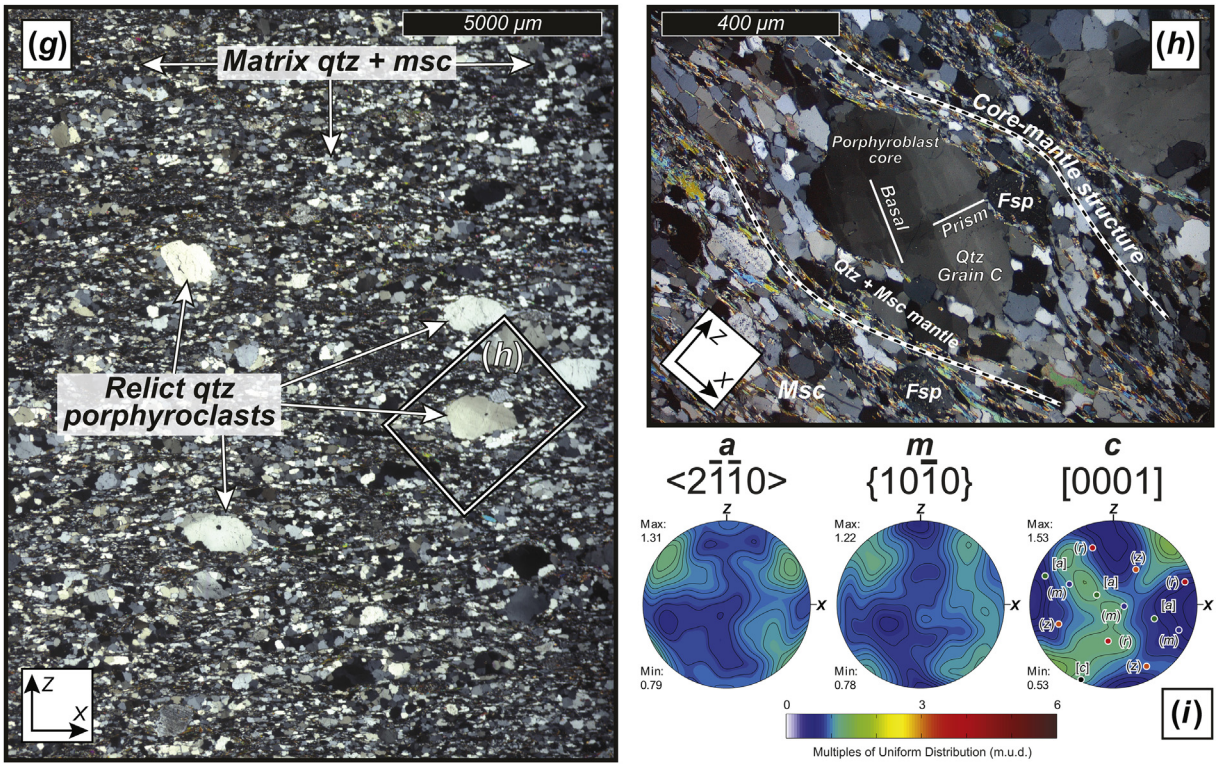

Fig. 2. (*continued*)

elliptical in shape (Fig. 2d). Quartz grain morphologies are typically dominated by microstructures associated with GBM (Fig. 2d–e). A minority of grains display evidence of partial annealing with straighter grain boundaries and no subgrains. Most grains contain subgrains (Fig. 2d), many of which are 200–400 μm wide chessboard subgrains (Fig. 2e), comparable to those in sample P12/017 (Fig. 2a). Small dihedral angles (< 60°) at quartz-feldspar and feldspar-feldspar grain-boundary triple junctions, isolated potassium feldspar neosomes, and feldspar or quartz pseudomorphs of melt-filled pores indicate that dynamic recrystallisation took place contemporaneously with partial melting (Parsons et al., 2016a). Quartz CPO, measured across the samples at a 14 μm step size, has a concentration of [*c*]-axes sub-parallel to *X*, suggestive of prism-[*c*] slip (Fig. 2f).

Quartz Grain B has a chessboard subgrain microstructure (Fig. 2d–e). In the top left corner of Quartz Grain B (Fig. 2e) two main sets of subgrain boundaries have traces parallel to those of the basal plane and the prism plane. In the bottom right corner of Quartz Grain B, subgrain boundaries are more complex; three orientations of subgrain boundaries are present, with traces parallel to those of the basal plane, prism planes, and rhomb planes (Fig. 2e). The orientation of Quartz Grain B differs from the whole rock CPO, having its [*c*]-axis subparallel to *Z* (Fig. 2f).

Crossed-girdle opening-angle thermometry of locally derived samples from the same rock unit (Parsons et al., 2016a) yielded quartz deformation temperatures of 631 ± 50 °C to 663 ± 50 °C based on the thermometer of Kruhl (1998, modified by Law, 2014) and 593 ± 50 °C to 621 ± 50 °C based on the thermometer of Faleiros et al. (2016). Petrology-based thermobarometry of sample P12/058 yielded a peak temperature and pressure of 703 ± 13 °C and 11.5 ± 1.3 kbar (Parsons et al., 2016c). Together, these constraints suggest that sample P12/058 preserves retrograde deformation from ~10–13 kbar and ~700 °C down to temperatures of ~550–600 °C.

3.3. P13/052M: micaceous quartzite, MCTZ

Sample P13/052M (Fig. 2g–i) is a micaceous quartzite from the MCTZ (Fig. 1). Quartz grains form microlithons sub-parallel to foliation and have a bimodal grain-size distribution, divided into smaller matrix grains and larger porphyroclasts (Fig. 2g). Quartz matrix grains are subhedral in shape with interlobate to polygonal grain boundaries (Fig. 2g). Polygonal static recrystallisation microstructures are common, although partially annealed dynamic recrystallisation microstructures indicative of subgrain rotation and rarer grain boundary bulging are preserved in some matrix grains (Fig. 2g). Quartz porphyroclasts are subhedral and elliptical, and commonly preserve 50–150 μm wide chessboard subgrains that are not observed in the matrix grains (Fig. 2g–h). Quartz CPO, measured across the sample at a 13 μm step size, is weak (Fig. 2i) and produces a poorly defined [*c*]-axis crossed-girdle fabric with a weak asymmetry suggestive of non-coaxial mixed < *a* > slip (Parsons et al., 2016a).

Quartz Grain C is a large porphyroclast with chessboard subgrain boundaries with traces parallel to those of the basal and prism planes (Fig. 2h). Subgrain boundaries with traces parallel to those of the rhombohedral planes are not observed in this grain. The [*c*]-axis of Quartz Grain C (Fig. 2i) lies between the *X* and *Z* directions, overlapping the strongest [*c*]-axis maximum of the whole-rock CPO (Fig. 2i).

Crossed-girdle opening-angle thermometry of this sample (Parsons et al., 2016a) yielded a quartz deformation temperature of 631 ± 50 °C based on the thermometer of Kruhl (1998, modified by Law, 2014) and 593 ± 50 °C based on the thermometer of Faleiros et al. (2016). Optically identified quartz deformation microstructures suggest quartz deformation temperatures of 400 to ≥650 °C (Parsons et al., 2016a). In this region, chessboard subgrains are reported from larger porphyroclasts in other samples collected from the MCTZ (Parsons et al., 2016a). Petrology-based thermobarometry from an equivalent structural level in a neighbouring valley yielded peak metamorphic conditions of ~500–600 °C and ~7–9 kbar (Martin et al., 2010; Corrie and Kohn, 2011). Together, these constraints suggest that sample P13/052M preserves retrograde deformation from ~7–9 kbar and ~550–650 °C down to temperatures of ~400–500 °C. These temperatures are lower than expected for the formation of the chessboard

subgrains (e.g. Kruhl, 1996) observed within the large porphyroclasts (e.g., Quartz Grain C, Fig. 2h), which probably derive from earlier, higher temperature deformation that is not recorded by the matrix grains. We suggest that these porphyroclasts either record pre-Himalayan high-temperature metamorphism of their metasedimentary protolith or are relict detrital grains from a high grade pre-Himalayan metamorphic sediment source.

4. Methods

4.1. EBSD data acquisition

Electron backscatter diffraction (EBSD) data were acquired on an FEI Quanta 650 FEG E-SEM in the Department of Earth Sciences, University of Oxford, equipped with Oxford Instruments AZtec 2.1 acquisition software and a NordlysNano EBSD camera. Reference frame conventions were validated following the approach of Britton et al. (2016). Diffraction patterns were collected from uncoated specimens in low-vacuum mode (50 Pa) to optimise pattern quality and minimise charging, and were saved for HR-EBSD post-processing. Diffraction patterns were collected without binning of pixels from the raw patterns to maximise pattern resolution. The characteristics of each dataset are summarised in Table 1. Relatively large step sizes of 5–8 μm were beneficial for characterising the large subgrain sizes present in the samples, keeping processing time for HR-EBSD to a minimum, and optimising resolution of orientation gradients (i.e., resolving subtle lattice curvature) (Jiang et al., 2013; Wallis et al., 2016). Although the apparent density of GNDs varies with both binning and step size, based on previous assessments, the differences in step size between maps of different samples are expected to have negligible impacts on the relative apparent GND densities between maps (Jiang et al., 2013; Wallis et al., 2016).

4.2. Estimating densities of geometrically necessary dislocations (GNDs) in quartz using HR-EBSD

4.2.1. Mapping lattice rotations with HR-EBSD

Conventional EBSD based on the Hough transform has two disadvantages when applied to small misorientation angles typical of intragranular substructure. First, the precision of measurements of misorientation angles is limited to ~0.2° by the process of determining band positions in Hough-space. This limited precision generates 'orientation noise' in estimates of densities of GNDs, placing a limit on the dislocation structures that can be resolved (Wilkinson and Randman, 2010; Wallis et al., 2016). Second, the error in determination of misorientation axes between individual orientation measurements increases with decreasing misorientation angle (Prior, 1999; Wilkinson, 2001). For instance, calculated misorientation axes can differ from true axes by tens of degrees for misorientation angles less than 10° (Kruse et al., 2001; Wilkinson, 2001). The average misorientation axis for a crystal can be determined with reasonable accuracy by consideration of a large number of points within the same grain (Prior, 1999). However, the problem remains for point-to-point misorientations from which GNDs are estimated. In particular, this issue makes it difficult to determine the specific types of GNDs present in distorted crystals (Wilkinson and Randman, 2010; Wallis et al., 2016). In contrast, HR-EBSD employs cross-correlation of diffraction patterns to measure lattice misorientation, and thereby circumvents the above limitations.

For HR-EBSD, the Hough transform is used only to determine the orientation of a single reference point in each grain. Misorientations between all other points in the grain are determined by cross-correlating regions of interest (ROI) in each diffraction pattern with the corresponding ROI in the pattern from the reference point. A vector, **r**, describing the position of a ROI in the reference pattern, relative to the point from which the pattern is generated, is related to a vector, **r′**, describing the position of the same feature in a test pattern by

$$\mathbf{r}' = (\mathbf{D} + \mathbf{I})\mathbf{r}, \tag{1}$$

where **I** is the identity matrix, and **D** is the displacement gradient tensor (Britton and Wilkinson, 2012). The displacement gradient tensor is defined as

$$\mathbf{D} = \begin{bmatrix} \frac{\partial u_1}{\partial x_1} & \frac{\partial u_1}{\partial x_2} & \frac{\partial u_1}{\partial x_3} \\ \frac{\partial u_2}{\partial x_1} & \frac{\partial u_2}{\partial x_2} & \frac{\partial u_2}{\partial x_3} \\ \frac{\partial u_3}{\partial x_1} & \frac{\partial u_3}{\partial x_2} & \frac{\partial u_3}{\partial x_3} \end{bmatrix}, \tag{2}$$

where x_i is a direction in the crystal and u_i is a displacement in the ith direction (Wilkinson et al., 2006; Britton and Wilkinson, 2011). Infinitesimal strains, ε_{ij}, and rotations, ω_{ij}, are represented by the symmetric and antisymmetric parts of **D,** respectively, by (Wilkinson et al., 2006)

$$\varepsilon_{ij} = \frac{1}{2}\left(\frac{\partial u_i}{\partial x_j} + \frac{\partial u_j}{\partial x_i}\right) \tag{3}$$

and

$$\omega_{ij} = \frac{1}{2}\left(\frac{\partial u_i}{\partial x_j} - \frac{\partial u_j}{\partial x_i}\right). \tag{4}$$

We used 100 ROI of 256 × 256 pixels each to calculate a field of displacement vectors that describe how the diffraction pattern at the reference point must be deformed to match the pattern at the point of interest (Britton and Wilkinson, 2011). This displacement vector field is then used to determine the best-fitting displacement gradient tensor. This approach provides precision in measurements of misorientation angles on the order of ~0.01°, whilst simultaneously retaining precision in the misorientation axes, even for misorientations less than 1° (Wilkinson et al., 2006). The original approach of Wilkinson et al. (2006) allows rotations and elastic strains to be recovered up to misorientation angles of ~8°, at which point features in the corresponding regions of interest in the reference and test patterns typically become too dissimilar for accurate analysis. Therefore, Britton and Wilkinson (2011, 2012) proposed a more robust iterative fitting routine and pattern remapping approach to allow determination of finite rotations (Ω_{ij}) and strains (E_{ij}) up to misorientation angles of ~11°. We employ this modification of the original method in this study due to the large rotations across subgrain boundaries.

4.2.2. Estimating densities of GNDs

Analysis of GNDs can be conducted through the 'dislocation tensor', **α**, using Nye-Kröner analysis (Nye, 1953; Kröner, 1958). The dislocation tensor can be derived from lattice rotations and strains by taking the curl of the elastic distortion,

Table 1
Characteristics of EBSD datasets.

Sample	Binning of pixels in diffraction patterns	Step size (μm)	Steps in X and Y
P12/017	none	5	182 × 125
P12/058	none	5	144 × 80
P13/052	none	8	92 × 67

$$\alpha = \begin{bmatrix} \frac{\partial \Omega_{12}}{\partial x_3} - \frac{\partial \Omega_{31}}{\partial x_2} & \frac{\partial \Omega_{13}}{\partial x_1} & \frac{\partial \Omega_{21}}{\partial x_1} \\ \frac{\partial \Omega_{32}}{\partial x_2} & \frac{\partial \Omega_{23}}{\partial x_1} - \frac{\partial \Omega_{21}}{\partial x_3} & \frac{\partial \Omega_{21}}{\partial x_2} \\ \frac{\partial \Omega_{32}}{\partial x_3} & \frac{\partial \Omega_{13}}{\partial x_3} & \frac{\partial \Omega_{31}}{\partial x_2} - \frac{\partial \Omega_{32}}{\partial x_1} \end{bmatrix} + \begin{bmatrix} \frac{\partial E_{12}}{\partial x_3} - \frac{\partial E_{13}}{\partial x_2} & \frac{\partial E_{13}}{\partial x_1} - \frac{\partial E_{11}}{\partial x_3} & \frac{\partial E_{11}}{\partial x_2} - \frac{\partial E_{12}}{\partial x_1} \\ \frac{\partial E_{22}}{\partial x_3} - \frac{\partial E_{23}}{\partial x_2} & \frac{\partial E_{23}}{\partial x_1} - \frac{\partial E_{21}}{\partial x_3} & \frac{\partial E_{21}}{\partial x_2} - \frac{\partial E_{22}}{\partial x_1} \\ \frac{\partial E_{32}}{\partial x_3} - \frac{\partial E_{33}}{\partial x_2} & \frac{\partial E_{33}}{\partial x_1} - \frac{\partial E_{31}}{\partial x_3} & \frac{\partial E_{31}}{\partial x_2} - \frac{\partial E_{32}}{\partial x_1} \end{bmatrix}, \quad (5)$$

and can be related to the densities, ρ^s, of s different types of dislocation, each with Burgers vector $\mathbf{b}^s$ and line direction $\mathbf{l}^s$, by

$$\alpha_{ij} = \sum_{s=1}^{s_{max}} \rho^s b_i^s l_j^s \quad (6)$$

(Field et al., 2005; Wilkinson and Randman, 2010). As the measured elastic strain gradients in our samples average ~1% of the rotation gradients, we follow the approach of Wilkinson and Randman (2010), in which the contribution from elastic strains is neglected and five of the nine elements of α_{ij} are determined directly, along with the difference between two of the elements ($\alpha_{11} - \alpha_{22}$) (Pantleon, 2008), from 2-dimensional EBSD maps. The problem of estimating the densities of each type of GND from the available components of α_{ij} can be set out as

$$\boldsymbol{\rho} = \mathbf{A}^{\mathrm{T}}(\mathbf{A}\mathbf{A}^{\mathrm{T}})^{-1}\boldsymbol{\Lambda} \quad (7)$$

where ρ is an s x 1 column vector in which each element represents the density of a particular dislocation type, $\boldsymbol{\Lambda}$ is a 6 × 1 column vector of measured orientation gradients, and $\mathbf{A}$ is a 6 × s_{max} matrix in which each column contains the dyadic of the Burgers vector and unit line direction of the sth dislocation type (Field et al., 2005; Wilkinson and Randman, 2010). If there are six or fewer dislocation types, then ρ can be calculated directly using equation (7), which minimizes the misfit between predicted and observed curvatures (Wallis et al., 2016). However, if there are more than six possible dislocation types, then ρ is under-constrained and an L1 optimisation scheme is used to find a solution that additionally minimizes some other objective variable, such as the total dislocation line energy (Wilkinson and Randman, 2010). For quartz we consider 19 dislocation types grouped into six families (Trépied et al., 1980; Lloyd et al., 1997; Toy et al., 2008; Morales et al., 2014) given in Table 2, and for simplicity we omit less common dislocation types (summarised in Lloyd et al., 1997). The energies of edge and screw dislocations, e_{edge} and e_{screw} respectively, used in the L1 minimisation scheme are in the ratio

$$\frac{e_{\mathrm{edge}}}{e_{\mathrm{screw}}} = \frac{1}{1-\nu}, \quad (8)$$

where ν is the Poisson's ratio. Poisson's ratios of quartz are rather low, $\nu \approx 0.1$ (Levien et al., 1980; McKnight et al., 2008), and therefore this approach is similar to minimising the total GND density. The optimisation algorithm used is for non-negative values only, i.e., all non-zero dislocation densities must be positive (Wallis et al., 2016). Therefore, we include both positive and negative signs of each Burgers vector, to be able to describe opposite senses of lattice curvature. We note that, with the chosen combination of slip systems, $\{m\}[c]$ edge and $[c]$ screw dislocations provide unique contributions to particular components of the dislocation tensor (i.e., only one dislocation type can generate a particular component of lattice curvature), as summarised in Table 3. In contrast, all dislocation types with $< a >$ Burgers vectors provide non-unique contributions to particular components of the dislocation tensor (i.e., more than one dislocation type could generate a particular component of lattice curvature) (Table 3). Therefore, estimated densities of dislocations with $[c]$ Burgers vectors are unique solutions, whilst densities of dislocations with $< a >$ Burgers vectors are non-unique. Although one cannot uniquely distinguish different dislocation types with $< a >$ Burgers vectors, all dislocations with $< a >$ Burgers vectors are distinguishable from those with $[c]$ Burgers vectors. Other approaches can also be used to investigate the dislocation content based on lattice curvature, such as the weighted Burgers vector analysis of Wheeler et al. (2009), and would also benefit from the improved angular resolution offered by HR-EBSD. Due to the possible presence of 'statistically stored dislocations' (e.g., dipoles) and lattice orientation gradients in the third dimension, any GND estimates based on a two-dimensional grid of orientation measurements provide a lower bound on the total dislocation density, unless combined with independent constraints.

Table 2
Dislocation families considered in GND analysis.

Dislocation family	Miller-Bravais index of slip planes (for edge dislocations only) and Burgers vectors	Number of symmetrically equivalent dislocation types
$(c) < a >$ edge	$(0001)\langle 11\bar{2}0\rangle$	3
$\{r/z\} < a >$ edge	$\{10\bar{1}1\}/\{01\bar{1}1\}$ $\langle 1\bar{2}10\rangle/\langle 2\bar{1}\bar{1}0\rangle$	6
$\{m\} < a >$ edge	$\{10\bar{1}0\}\langle 1\bar{2}10\rangle$	3
$\{m\}[c]$ edge	$\{10\bar{1}0\}[0001]$	3
$< a >$ screw	$\langle 11\bar{2}0\rangle$	3
$[c]$ screw	$[0001]$	1

Table 3
Dislocation types that can contribute to each component of the dislocation tensor (α_{ij}) if an [a]-axis is aligned with the 1-direction and the [c]-axis is aligned with the 3-direction.

	α_{i1}	α_{i2}	α_{i3}
α_{1j}	$(c) < a >$, $\{r/z\} < a >$, $< a >$ screw	$(c) < a >$, $\{r/z\} < a >$, $< a >$ screw	$\{r/z\} < a >$, $\{m\} < a >$
α_{2j}	$(c) < a >$, $\{r/z\} < a >$, $< a >$ screw	$(c) < a >$, $\{r/z\} < a >$, $< a >$ screw	$\{r/z\} < a >$, $\{m\} < a >$
α_{3j}	$\{m\}[c]$	$\{m\}[c]$	$[c]$ screw

5. Results

Lattice rotations relative to the reference points within each of the mapped grains are presented in Fig. 3. Each sample contains a complex substructure with steep rotation gradients corresponding to subgrain boundaries. Typical spacings of these boundaries are on the order of 100 μm. Maximum rotations across the mapped regions are up to approximately 0.2 rad (~11°) in P12/052M, i.e., approaching the maximum intragranular orientation range of HR-EBSD (Britton and Wilkinson, 2011). Typical rotations between adjacent subgrains are on the order of 0.01 rad (< 1°). Sets of subgrain boundaries with traces approximately parallel to the traces of the basal and prism planes are evident in each mapped area. Samples P12/017 and P12/058 also contain some boundaries with traces oblique to those of the basal and prism planes.

Estimated GND densities in samples P12/017, P12/058, and P13/052M are presented in Figs. 4–6, respectively. Maps of total GND density in each sample exhibit angular arrays of subgrain boundaries containing GND densities averaging approximately 10^{13} m^{-2}. Subgrain boundaries are typically straight or gently curved, their traces aligned approximately parallel to the basal and prism planes, and exhibit numerous ~90° corners and junctions. In P12/058 some subgrain boundaries are kinked, exhibit non-90° angles, or are oblique to the prism and basal planes. Subgrain interiors typically have GND densities of ≤ 10^{12} m^{-2}.

Dislocations with both $[c]$ and $< a >$ Burgers vectors are present in the subgrain boundaries (Figs. 4–6). $\{m\}[c]$ edge dislocations make the greatest contribution to boundaries with traces approximately parallel to the basal plane in samples P12/058 and P13/052M (Figs. 5 and 6). In sample P12/017, $\{m\}[c]$ edge dislocations again contribute to the basal

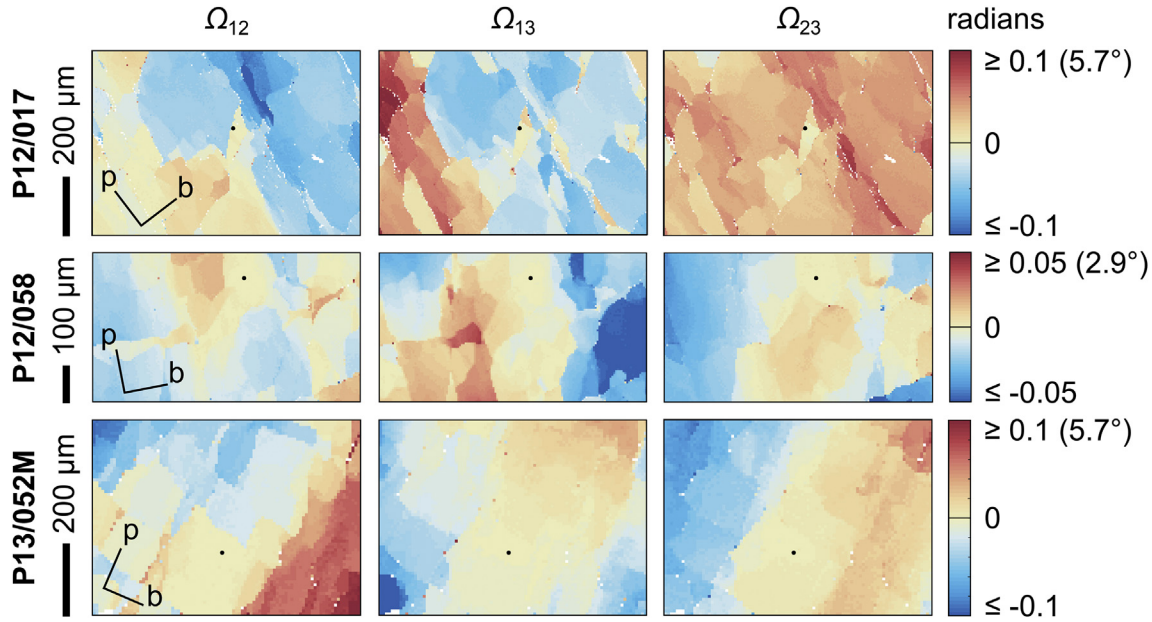

Fig. 3. Components of the finite rotation matrix (Ω_{ij}) describing lattice rotations relative to the crystal orientation at the reference point (black) in each grain. The approximate traces of the basal (b) and prism (p) planes are indicated, but these vary by a few degrees across the map areas due to misorientation across subgrain boundaries. Discontinuities in the rotation fields result from subgrain boundaries and correspond to high densities of GNDs in Figs. 4–6.

subgrain boundaries but are accompanied by similar densities of dislocations with < *a* > Burgers vectors (Fig. 4). Boundaries with traces approximately parallel to the prism planes are composed primarily of dislocations with < *a* > Burgers vectors. Of the dislocations with < *a* > Burgers vectors, screw dislocations appear in the highest densities, although most boundaries contain multiple dislocation types.

6. Discussion

6.1. The dislocation structure of chessboard subgrain boundaries in quartz revealed by HR-EBSD

It is difficult to distinguish the specific dislocation types that comprise chessboard subgrain boundaries in natural quartz using previously employed techniques. The most common techniques applied to analyse chessboard microstructures are (1) visible light microscopy using a universal stage microscope, which can only measure the angle between the [*c*]-axis and the plane of a subgrain boundary (Blumenfeld et al., 1986; Okudaira et al., 1995; Kruhl, 1996), and (2) EBSD, which suffers from limited precision in measurements of small misorientation angles and axes (Prior, 1999; Wilkinson, 2001; Britton and Wilkinson, 2011). Both techniques provide limited accuracy to determine the types and densities of GNDs within chessboard subgrain boundaries, which are typically characterised by small misorientation of only a few degrees (Fig. 3). Mainprice et al. (1986) analysed chessboard subgrain boundaries using transmission electron microscopy and identified boundaries of predominantly tilt character composed of dislocations with Burgers vectors parallel to [*c*] (basal subgrain boundaries) and < *a* > (prismatic subgrain boundaries). However, transmission electron microscopy is restricted to small sample volumes and therefore the structure of chessboard subgrain boundaries across multiple subgrains has remained poorly characterised. The use of HR-EBSD, based on cross-correlation of diffraction patterns, enables significantly more precise measurement of misorientation angles and axes than possible with conventional EBSD, allowing the dislocation types and densities that make-up chessboard subgrain boundaries to be analysed and quantified in new detail over sample areas sufficient for characterisation of large subgrains.

Our results indicate that in general chessboard subgrain boundaries with traces approximately parallel to the basal plane are composed primarily of {*m*}[*c*] edge dislocations (and therefore have strong tilt components). In contrast, subgrain boundaries with traces approximately parallel to prism planes are composed primarily of dislocations with < *a* > Burgers vectors (Figs. 4–6). These observations are consistent with the original definitions of chessboard subgrains (Mainprice et al., 1986; Kruhl, 1996; Lloyd et al., 1997), thus ruling out the possibility that they are 'pseudo-chessboard subgrains' (see Kruhl, 1996). However, the abundance of < *a* > screw dislocations, particularly within boundaries with traces approximately parallel to prism planes, suggested by our analysis is in contrast to TEM observations that both sets of boundaries have dominantly tilt character (Mainprice et al., 1986). As noted in Section 4.2.2., solutions involving lattice curvature components associated with dislocations with < *a* > Burgers vectors are non-unique (Table 3) and the energy minimisation approach used to choose a solution favours screw dislocations (equation (8)). Therefore, it remains possible that edge dislocations with < *a* > Burgers vectors may be present in greater densities than revealed by the present approach. These observations highlight the need to scrutinise carefully the relative densities of screw and edge dislocations and the benefits of combining information from multiple techniques. We note that this ambiguity would be present for any analysis based only on lattice orientation data regardless of the measurement technique. Nonetheless, the development and application of the HR-EBSD method to quartz opens new opportunities to quantitatively analyse its intragranular deformation microstructures, particularly those composed of low dislocation densities.

6.2. Chessboard subgrains in quartz as indicators of deformation conditions

The results of our HR-EBSD analysis corroborate previous interpretations that the development of chessboard subgrains in quartz requires the formation and glide of prism-[*c*] edge dislocations, and their climb into tilt-dominated basal subgrain boundaries (Blumenfeld et al., 1986; Mainprice et al., 1986; Okudaira et al., 1995; Kruhl, 1996; Little et al., 2013). Kruhl (1996) proposed that at pressures up to ~10 kbar, chessboard subgrains only develop within the pressure-temperature (PT) stability field of β-quartz (Van Groos and Ter Heege, 1973) and can thereby be used as a deformation geothermobarometer.

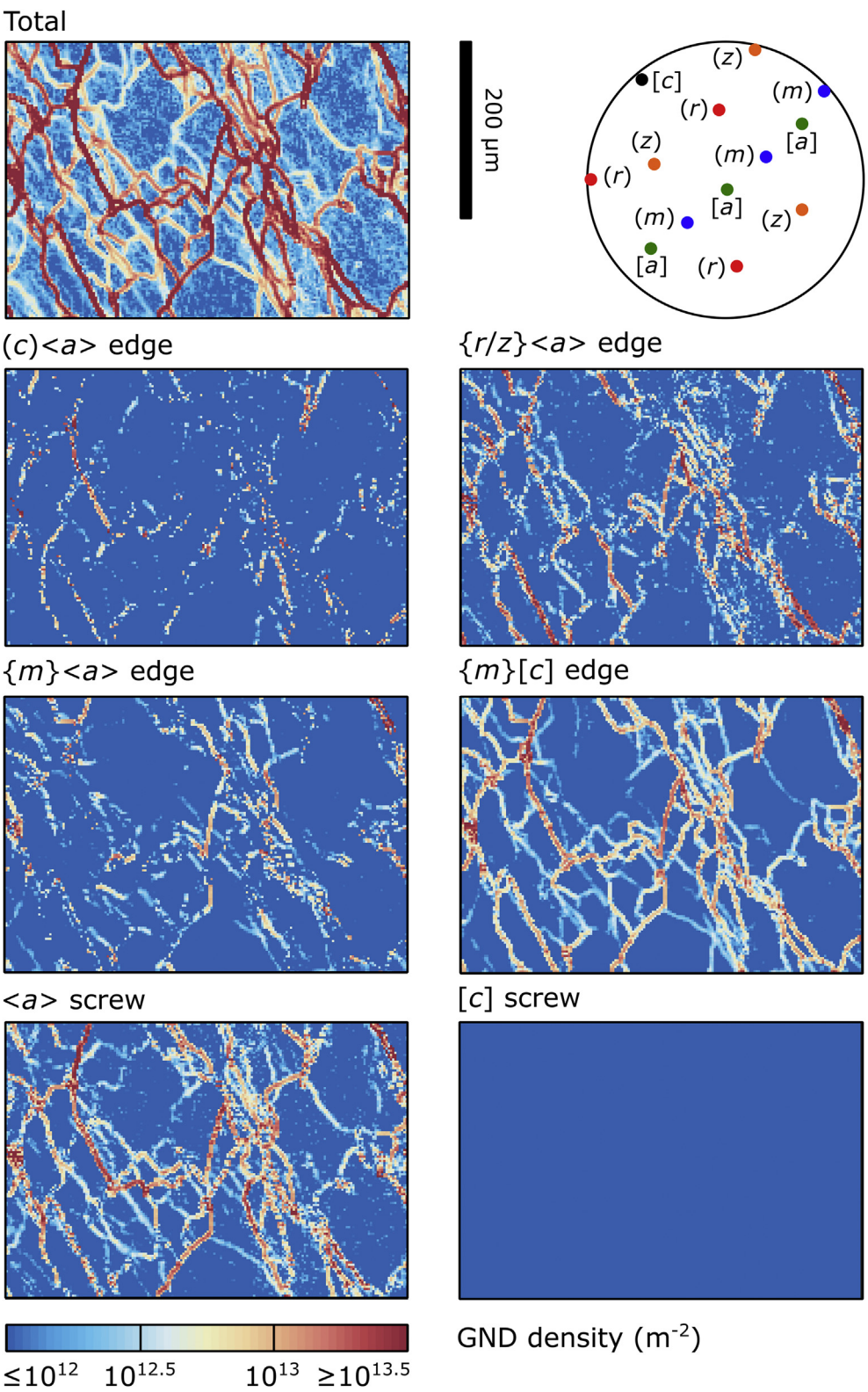

Fig. 4. Densities of geometrically necessary dislocations determined by HR-EBSD analysis of Quartz Grain A in micaceous quartzite sample P12/017 (UGHS). Results are presented as maps of the density of each type of dislocation, and also the sum of all dislocation types. Pole figure indicates the mean orientation of the grain within the mapped area.

Additionally, recent analyses of quartz [*c*]-axis CPOs developed across a range of temperatures led Faleiros et al. (2016) to propose that prism-[*c*] slip becomes the dominant slip system at deformation temperatures of > 700 °C. Both Mainprice et al. (1986) and Faleiros et al. (2016) correlated this dominance of prism-[*c*] slip at > 650–700 °C to the transition from α-quartz to β-quartz (Van Groos and Ter Heege, 1973). However, these conclusions have been questioned by Okudaira et al. (1998) who pointed out observations of microstructures indicative of prism-[*c*] slip that developed within the stability field of α-quartz (Lister and Dornsiepen, 1982; Garbutt and Teyssier, 1991; Okudaira et al., 1995).

PT conditions recorded within the UGHS in the Annapurna-Dhaulagiri region (purple PT path, Fig. 1c) indicate that samples P12/058 and P12/017 were never at conditions equivalent to the β-quartz

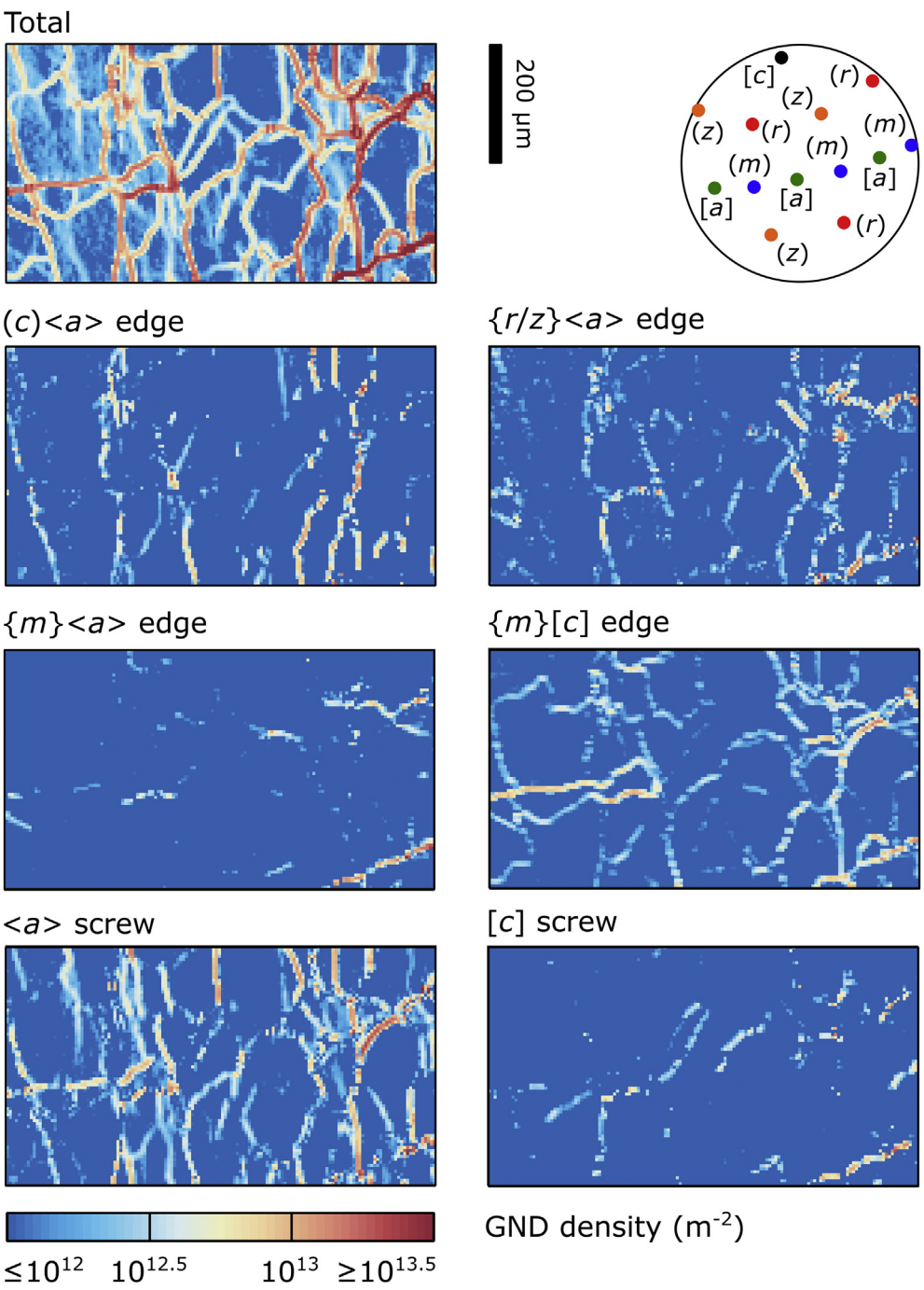

Fig. 5. Densities of geometrically necessary dislocations determined by HR-EBSD analysis of Quartz Grain B in pelitic paragneiss sample P12/058 (UGHS). Results are presented as maps of the density of each type of dislocation, and also the sum of all dislocation types. Pole figure indicates the mean orientation of the grain within the mapped area.

stability field. Likewise, many occurrences of chessboard subgrains reported from the GHS elsewhere in the Himalaya (e.g. Langille et al., 2010; Spencer et al., 2012; Larson and Cottle, 2014; Long et al., 2016) occur in areas where regional PT constraints fall mostly or entirely within the α-quartz stability field (pink PT path, Fig. 1c). Comparisons of single quartz grain orientations and whole rock quartz CPOs (Fig. 2c,f) suggest that the preserved chessboard subgrains in Quartz Grains A and B are unrelated to the whole-rock CPOs, which likely formed on the retrograde path. These chessboard subgrains probably formed during earlier deformation of these samples at or close to peak metamorphic conditions (Quartz Grain C in P13/052M is excluded from this discussion as it may be a relict grain preserving a pre-Himalaya deformation for which we have no PT constraints). Assuming that 1) the aforementioned PT paths are correct and 2) if at pressures below ~10 kbar chessboard subgrains may only form in the β-quartz stability field (Kruhl, 1996), then the described PT constraints suggest that at pressures *above* ~10 kbar, chessboard subgrain formation and activity of prism-[*c*] slip may occur within the α-quartz stability field (e.g., Fig. 1c).

Activity of prism-[*c*] slip in naturally deformed quartz has been inferred to be enabled or promoted in the presence of water-rich fluids and/or intracrystalline hydrous defects (Lister and Dornsiepen, 1982; Blumenfeld et al., 1986; Mainprice et al., 1986; Garbutt and Teyssier, 1991; Okudaira et al., 1995). Prism-[*c*] slip has also been activated in deformation experiments conducted at high temperatures on wet synthetic quartz and hydrothermally treated natural quartz (Baëta and Ashbee, 1969; Blacic, 1975; Linker et al., 1984; Muto et al., 2011). Experimental observations also suggest that the onset of prism-[*c*] slip occurs at lower temperatures as the water content of quartz increases (Blacic, 1975). Moreover, the onset of prism-[*c*] slip coincides with the

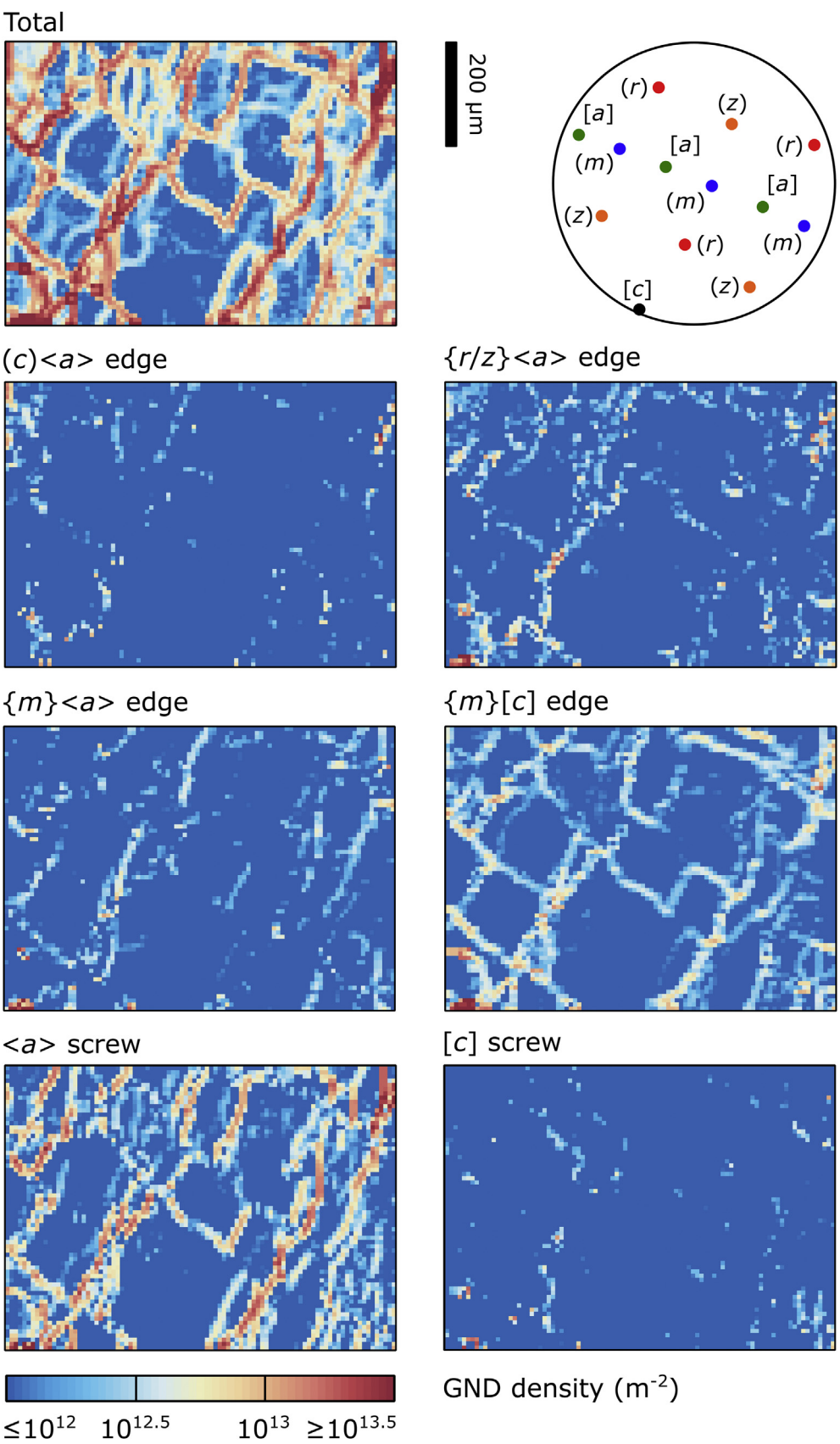

Fig. 6. Densities of geometrically necessary dislocations determined by HR-EBSD analysis of Quartz Grain C in micaceous quartzite sample P13/052M (MCTZ). Results are presented as maps of the density of each type of dislocation, and also the sum of all dislocation types. Pole figure indicates the mean orientation of the grain within the mapped area.

critical temperature for hydrolytic weakening (Blacic, 1975), and glide in the [*c*] direction is more rapid than glide in the < *a* > directions at a given temperature in wet quartz (Linker et al., 1984). In contrast, prism-[*c*] slip is only rarely activated in experiments on dry natural quartz (Blacic, 1975), in which it can fail to activate despite being optimally oriented for slip (Stünitz et al., 2017). Despite such

observations, the precise controls on the activity of prism-[*c*] slip (e.g. water weakening, temperature, applied stress), and hence the development of chessboard subgrains, remain poorly constrained.

Our HR-EBSD analyses demonstrate that chessboard subgrains in quartz-rich samples from the UGHS developed through activation of prism-[*c*] slip during deformation at or close to peak metamorphic conditions. The inference that prism-[*c*] slip in quartz is indicative of dislocation creep under hydrous conditions suggests that the rheology of quartz-rich domains of the UGHS may be described appropriately by a 'wet' quartzite flow law (Gleason and Tullis, 1995). Parsons et al. (2016c) demonstrated that at peak temperatures, viscosity estimates for deformation of quartz-rich domains in the UGHS determined from this flow law were equivalent to the viscosity required to numerically simulate mid-crustal channel flow (10^{19} Pa s, Beaumont et al., 2004). As such, the reduction in viscosity needed for mid-to lower-crustal channel flow may not be as dependent on the occurrence of partial melting as previously suggested, and may be achieved through high-temperature solid-state ductile flow of wet quartz-rich domains of the mid-crust (e.g. Le Pape et al., 2015; Parsons et al., 2016c). This hypothesis is one such example highlighting the need for further investigations of the controls of prism-[*c*] slip and the effects of water on the mechanical and rheological behaviour of quartz and quartz-rich lithologies.

7. Conclusions

This study provides the first detailed characterisation of the types and densities of geometrically necessary dislocations in quartz using HR-EBSD. This method is based on cross-correlation of diffraction patterns and provides improved resolution of misorientation angles and axes compared to conventional EBSD, which aid characterisation of GND densities and types respectively. We applied the method to chessboard subgrains from the Greater Himalayan Sequence in the Annapurna-Dhaulagiri Himalaya, Nepal, to provide quantitative estimates of the densities of different dislocation types present in subgrain boundaries that constitute chessboard subgrain microstructures in quartz. Subgrain boundaries with traces approximately parallel to the basal plane contain high densities of {*m*}[*c*] edge dislocations, whereas boundaries with traces approximately parallel to the prism planes are dominated by dislocations with $< a >$ Burgers vectors, although we are unable to uniquely determine the relative contributions of $< a >$ screw versus $< a >$ edge dislocations. Apparent GND densities within the boundaries are on the order of 10^{13} m^{-2}. These findings are broadly consistent with previous studies of quartz chessboard subgrains based on optical and transmission electron microscopy but provide quantitative characterisation over larger sample areas for the first time. The results suggest that at pressures > 10 kbar, chessboard subgrains may form within the α-quartz stability field. Importantly, the application of HR-EBSD to quartz and other geological minerals presents a wealth of new opportunities for quantitative characterisation of deformation microstructures.

Acknowledgements

We thank Holger Stünitz, Jörn Kruhl and Editor Joao Hippertt for helpful reviews. We are grateful to Geoff Lloyd, Rick Law, Mike Searle, and Richard Phillips for many helpful discussions on quartz deformation and the geology of the Himalaya. We thank Angus Wilkinson and Ben Britton for assistance with HR-EBSD. D. Wallis and L.N. Hansen acknowledge support from the Natural Environment Research Council Grant NE/M000966/1. A.J. Parsons acknowledges support from the Natural Environment Research Council (training grant NE/J50001X/1).

References

Ábalos, B., Puelles, P., Fernández-Armas, S., Sarrionandia, F., 2011. EBSD microfabric study of pre-Cambrian deformations recorded in quartz pebbles from the Sierra de la Demanda (N Spain). J. Struct. Geol. 33 (4), 500–518. http://dx.doi.org/10.1016/j.jsg.2011.01.005.

Baëta, R.D., Ashbee, K.H.G., 1969. Slip systems in quartz: I. Experiments. Am. Mineral. 54, 1551–1573.

Beaumont, C., Jamieson, R.A., Nguyen, M.H., Medvedev, S., 2004. Crustal channel flows: 1. Numerical models with applications to the tectonics of the Himalayan-Tibetan orogen. J. Geophys. Res. Solid Earth 109, B6. http://dx.doi.org/10.1029/2003JB002809.

Blacic, J.D., 1975. Plastic-deformation mechanisms in quartz: the effect of water. Tectonophysics 27, 271–294. http://dx.doi.org/10.1016/0040-1951(75)90021-9.

Blumenfeld, P., Mainprice, D., Bouchez, J.L., 1986. C-slip in quartz from subsolidus deformed granite. Tectonophysics 127, 97–115. http://dx.doi.org/10.1016/0040-1951(86)90081-8.

Boneh, Y., Wallis, D., Hansen, L.N., Krawczynski, M.J., Skemer, P., 2017. Oriented grain growth and modification of 'frozen anisotropy' in the lithospheric mantle. Earth Planet Sci. Lett. 474, 368–374. http://dx.doi.org/10.1016/j.epsl.2017.06.050.

Britton, T.B., Wilkinson, A.J., 2011. Measurement of residual elastic strain and lattice rotations with high resolution electron backscatter diffraction. Ultramicroscopy 111, 1395–1404. http://dx.doi.org/10.1016/j.ultramic.2011.05.007.

Britton, T.B., Wilkinson, A.J., 2012. High resolution electron backscatter diffraction measurements of elastic strain variations in the presence of larger lattice rotations. Ultramicroscopy 114, 82–95. http://dx.doi.org/10.1016/j.ultramic.2012.01.004.

Britton, T.B., Jiang, J., Vilalta-Clemente, A., Wallis, D., Hansen, L.N., Winkelmann, A., Wilkinson, A.J., 2016. Tutorial: crystal orientations and EBSD — or which way is up? Mater. Char. 117, 113–126. http://dx.doi.org/10.1016/j.matchar.2016.04.008.

Caddick, M.J., 2005. Tectono-metamorphic Evolution of the Central and Western Himalaya. [Ph.D. thesis]. University of Cambridge.

Corrie, S.L., Kohn, M.J., 2011. Metamorphic history of the central Himalaya, Annapurna region, Nepal, and implications for tectonic models. Geol. Soc. Am. Bull. 123 (9–10), 1863–1879. http://dx.doi.org/10.1130/B30376.1.

Daniel, C.G., Hollister, L.S., Parrish, R.R., Grujic, D., 2003. Exhumation of the main central thrust from lower crustal depths, eastern Bhutan Himalaya. J. Metamorph. Geol. 21, 317–334. http://dx.doi.org/10.1046/j.1525-1314.2003.00445.x.

Faleiros, F.M., Moraes, R., Pavan, M., Campanha, G.A.C., 2016. A new empirical calibration of the quartz c-axis fabric opening-angle deformation thermometer. Tectonophysics 671, 173–182. http://dx.doi.org/10.1016/j.tecto.2016.01.014.

Field, D.P., Trivedi, P.B., Wright, S.I., Kumar, M., 2005. Analysis of local orientation gradients in deformed single crystals. Ultramicroscopy 103, 33–39. http://dx.doi.org/10.1016/j.ultramic.2004.11.016.

Garbutt, J.M., Teyssier, C., 1991. Prism < *c* > slip in the quartzites of the Oakhurst Mylonite belt, California. J. Struct. Geol. 13, 657–666. http://dx.doi.org/10.1016/0191-8141(91)90028-H.

Gleason, G.C., Tullis, J., 1995. A flow law for dislocation creep of quartz aggregates determined with the molten salt cell. Tectonophysics 247 (1), 1–23.

Harris, N.B.W., Caddick, M., Kosler, J., Goswami, S., Vance, D., Tindle, A.G., 2004. The pressure-temperature-time path of migmatites from the Sikkim Himalaya. J. Metamorph. Geol. 22, 249–264. http://dx.doi.org/10.1111/j.1525-1314.2004.00511.x.

Iaccarino, S., Montomoli, C., Carosi, R., Massonne, H.J., Langone, A., Visonà, D., 2015. Pressure–temperature–time–deformation path of kyanite-bearing migmatitic paragneiss in the Kali Gandaki valley (Central Nepal): investigation of Late Eocene–Early Oligocene melting processes. Lithos 231, 103–121. http://dx.doi.org/10.1016/j.lithos.2015.06.005.

Imayama, T., Takeshite, T., Yi, K., Cho, D.-L., Kitajima, K., Tsutsumi, Y., Kayama, M., Nishido, H., Okumura, T., Yagi, K., Itaya, T., Sano, Y., 2012. Two-stage partial melting and contrasting cooling history within the Higher Himalayan Crystalline Sequence in the far-eastern Nepal Himalaya. Lithos 134–135, 1–22. http://dx.doi.org/10.1016/j.lithos.2011.12.004.

Jiang, J., Britton, T.B., Wilkinson, A.J., 2013. Measurement of geometrically necessary dislocation density with high resolution electron backscatter diffraction: effects of detector binning and step size. Ultramicroscopy 125, 1–9. http://dx.doi.org/10.1016/j.ultramic.2012.11.003.

Kröner, E., 1958. Continuum theory of dislocations and self-stresses. Ergebnisse der Angewandten Mathematik 5, 1327–1347.

Kruhl, J.H., 1996. Prism- and basal-plane parallel subgrain boundaries in quartz: a microstructural geothermobarometer. J. Metamorph. Geol. 14, 581–589. http://dx.doi.org/10.1046/j.1525-1314.1996.00413.x.

Kruhl, J.H., 1998. Reply: prism- and basal-plane parallel subgrain boundaries in quartz: a microstructural geothermobarometer. J. Metamorph. Geol. 16 (1), 142–146.

Kruse, R., Stünitz, H., Kunze, K., 2001. Dynamic recrystallization processes in plagioclase porphyroclasts. J. Struct. Geol. 23, 1781–1802. http://dx.doi.org/10.1016/S0191-8141(01)00030-X.

Kumamoto, K.M., Thom, C.A., Wallis, D., Hansen, L.N., Armstron, D.E.J., Warren, J.M., Goldsby, D.L., Wilkinson, A.J., 2017. Size effects resolve discrepencies in 40 years of work on low-temperature plasticity in olivine. Sci. Adv. 3, e1701338. http://dx.doi.org/10.1126/sciadv.1701338.

Langille, J.M., Jessup, M.J., Cottle, J.M., Newell, D., Seward, G., 2010. Kinematic evolution of the Ama Drime detachment: insights into orogen-parallel extension and exhumation of the Ama Drime Massif, Tibet–Nepal. J. Struct. Geol. 32, 900–919. http://dx.doi.org/10.1016/j.jsg.2010.04.005.

Larson, K.P., Cottle, J.M., 2014. Midcrustal discontinuities and the assembly of the Himalayan midcrust. Tectonics 33, 718–740. http://dx.doi.org/10.1002/2013TC003452.

Law, R.D., 2014. Deformation thermometry based on quartz *c*-axis fabrics and recrystallisation microstructures: a review. J. Struct. Geol. 66, 129–161. http://dx.doi.org/10.1016/j.jsg.2014.05.023.

Le Pape, F., Jones, A.G., Unsworth, M.J., Vozar, J., Wei, W., Sheng, J., Ye, G., Jing, J., Dong, H., Zhang, L., Xie, C., 2015. Constraints on the evolution of crustal flow beneath Northern Tibet. Geochem. Geophys. Geosys. 16, 4237–4260. http://dx.doi.org/10.1002/2015GC005828.

Levien, L., Prewitt, C.T., Weidner, D.J., 1980. Structure and elastic properties of quartz at pressure. Am. Mineral. 65, 920–930.

Linker, M.F., Kirby, S.H., Ord, A., Christie, J.M., 1984. Effects of compression direction on the plasticity and rheology of hydrolytically weakened synthetic quartz crystals at atmospheric pressure. J. Geophys. Res. Solid Earth 89 (B6), 4241–4255. http://dx.doi.org/10.1029/JB089iB06p04241.

Lister, G.S., Dornsiepen, U.F., 1982. Fabric transitions I the Saxony granulite terrain. J. Struct. Geol. 4, 81–92. http://dx.doi.org/10.1016/0191-8141(82)90009-8.

Little, T.A., Hacker, B.R., Brownlee, S.J., Seward, G., 2013. Microstructures and quartz lattice-preferred orientations in the eclogite-bearing migmatitic gneisses of the D-Entrecasteaux Islands, Papua New Guinea. Geochem. Geophys. Geosys. 14, 2030–2062. http://dx.doi.org/10.1002/ggge.20132.

Lloyd, G.E., Farmer, A.B., Mainprice, D., 1997. Misorientation analysis and the formation and orientation of subgrain and grain boundaries. Tectonophysics 279, 55–78. http://dx.doi.org/10.1016/S0040-1951(97)00115-7.

Long, S.P., Gordon, S.M., Young, J.P., Soignard, E., 2016. Temperature and strain gradients through Lesser Himalayan rocks and across the Main Central thrust, south central Bhutan: implications for transport-parallel stretching and inverted metamorphism. Tectonics 35 (8), 1863–1891. http://dx.doi.org/10.1002/2016tc004242.

Mainprice, D., Bouchez, J.-L., Blumenfeld, P., Tubià, J.M., 1986. Dominant *c* slip in naturally deformed quartz: implications for dramatic plastic softening at high temperature. Geology 14, 819–822. http://dx.doi.org/10.1130/0091-7613(1986)14<819:DCSIND>2.0.CO;2.

Martin, A.J., Ganguly, J., Decelles, P.G., 2010. Metamorphism of greater and lesser Himalayan rocks exposed in the Modi Khola valley, central Nepal. Contrib. Mineral. Petrol. 159 (2), 203–223. http://dx.doi.org/10.1007/s00410-009-0424-3.

McKnight, R.E.A., Moxon, T., Buckley, A., Taylor, P.A., Darling, T.W., Carpenter, M.A., 2008. Grain size dependence of elastic anomalies accompanying the α–β phase transition in polycrystalline quartz. J. Phys. Condens. Matter 20, 075229. http://dx.doi.org/10.1018/0953-8984/20/7/075229.

Morales, L.F.G., Lloyd, G.E., Mainprice, D., 2014. Fabric transitions in quartz via viscoplastic self-consistent modeling part I: axial compression and simple shear under constant strain. Tectonophysics 636, 52–69. http://dx.doi.org/10.1016/j.tecto.2014.08.011.

Mottram, C.M., Parrish, R.R., Regis, D., Warren, C.J., Argles, T.W., Harris, N.B.W., Roberts, N.M.W., 2015. Using U-Th-Pb petrochronology to determine rates of ductile thrusting: time windows into the Main Central Thrust, Sikkim Himalaya. Tectonics 34, 1355–1374. http://dx.doi.org/10.1002/2014TC003743.

Muto, J., Hirth, G., Heilbronner, R., Tullis, J., 2011. Plastic anisotropy and fabric evolution in sheared and recrystallized quartz single crystals. J. Geophys. Res. Solid Earth 116, B02206. http://dx.doi.org/10.1029/2010JB007891.

Nye, J.F., 1953. Some geometrical relations in dislocated crystals. Acta Metall. 1, 153–162. http://dx.doi.org/10.1016/0001-6160(53)90054-6.

Okudaira, T., Takeshita, T., Hara, I., Ando, J., 1995. A new estimate of the conditions for transition from basal < *a* > to prism [*c*] slip in naturally deformed quartz. Tectonophysics 250, 31–46. http://dx.doi.org/10.1016/0040-1951(95)00039-4.

Okudaira, T., Takeshita, T., Toriumi, M., 1998. Discussion: prism- and basal-plane parallel subgrain boundaries in quartz: a microstructural geothermobarometer. J. Metamorph. Geol. 16, 141–142. http://dx.doi.org/10.111/j.1525-1314.1998.00063.x.

Pantleon, W., 2008. Resolving the geometrically necessary dislocation content by conventional electron backscattering diffraction. Scripta Mater. 58, 994–997. http://dx.doi.org/10.1016/j.scriptamat.2008.01.050.

Parsons, A.J., Law, R.D., Lloyd, G.E., Phillips, R.J., Searle, M.P., 2016a. Thermo-kinematic evolution of the Annapurna-Dhaulagiri Himalaya, central Nepal: the composite orogenic system. Geochem. Geophys. Geosys. 17 (4), 1511–1539. http://dx.doi.org/10.1002/2015gc006184.

Parsons, A.J., Law, R.D., Searle, M.P., Phillips, R.J., Lloyd, G.E., 2016b. Geology of the Dhaulagiri-Annapurna-Manaslu Himalaya, western region, Nepal. 1:200,000. J. Maps 12 (1), 100–110. http://dx.doi.org/10.1080/17445647.2014.984784.

Parsons, A.J., Phillips, R.J., Lloyd, G.E., Law, R.D., Searle, M.P., Walshaw, R.D., 2016c. Mid-crustal deformation of the Annapurna-Dhaulagiri Himalaya, central Nepal: an atypical example of channel flow during the Himalayan orogeny. Geosphere 12 (3), 985–1015. http://dx.doi.org/10.1130/ges01246.1.

Parsons, A.J., Ferré, E.C., Law, R.D., Lloyd, G.E., Phillips, R.J., Searle, M.P., 2016d. Orogen-parallel deformation of the Himalayan midcrust: insights from structural and magnetic fabric analyses of the greater Himalayan sequence, Annapurna-Dhaulagiri Himalaya, central Nepal. Tectonics 35, 2515–2537. http://dx.doi.org/10.1002/2016TC004244.

Prior, D.J., 1999. Problems in determining the misorientation axes, for small angular misorientations, using electron backscatter diffraction in the SEM. J. Microsc. 195, 217–225. http://dx.doi.org/10.1046/j.1365-2818.1999.00572.x.

Puelles, P., Ábalos, B., García De Madinabeitia, S., Sánchez-Lorda, M.E., Fernández-Armas, S., Gil Ibarguchi, J.I., 2014. Provenance of quartz-rich metamorphic tectonite pebbles from the "Black Flysch" (W Pyrenees, N Spain): an EBSD and detrital zircon LA–ICP-MS study. Tectonophysics 632, 123–137. http://dx.doi.org/10.1016/j.tecto.2014.06.004.

Searle, M.P., 2015. Mountain building, tectonic evolution, rheology, and crustal flow in the Himalaya, Karakoram, and Tibet. In: second ed. In: Schubert, G. (Ed.), Treatise on Geophysics, vol. 6. Elsevier, Oxford, pp. 469–511.

Spencer, C.J., Harris, R.A., Dorais, M.J., 2012. The metamorphism and exhumation of the Himalayan metamorphic core, eastern Garhwal region, India. Tectonics 31 (1). http://dx.doi.org/10.1029/2010tc002853. TC1007.

Stipp, M., Stünitz, H., Heilbronner, R., Schmid, S.M., 2002. The eastern Tonale fault zone: a 'natural laboratory' for crystal plastic deformation of quartz over a temperature range from 250 to 700 °C. J. Struct. Geol. 24, 1861–1884. http://dx.doi.org/10.1016/S0191-8141(02)00035-4.

Stünitz, H., Thust, A., Heilbronner, R., Behrens, H., Kilian, R., Tarantola, A., Fitz Gerald, J.D., 2017. Water redistribution in experimentally deformed natural milky quartz single crystals—implications for H_2O-weakening processes. J. Geophys. Res.: Solid Earth 122, 866–894. http://dx.doi.org/10.1002/2016JB013533.

Toy, V.G., Prior, D.J., Norris, R.J., 2008. Quartz fabrics in the Alpine Fault mylonites: influence of pre-existing preferred orientations on fabric development during progressive uplift. J. Struct. Geol. 30, 602–621. http://dx.doi.org/10.1016/j.jsg.2008.01.001.

Trépied, L., Doukhan, J.C., Paquet, J., 1980. Subgrain boundaries in quartz theoretical analysis and microscopic observations. Phys. Chem. Miner. 5, 201–218. http://dx.doi.org/10.1007/BF00348570.

Tubia, J.M., Cuevas, J., 1986. High-temperature emplacement of the Los Reales peridotite nappe (Betic Corillera, Spain). J. Struct. Geol. 8, 473–482. http://dx.doi.org/10.1016/0191-8141(86)90064-7.

Van Groos, A.F.K., Ter Heege, J.P., 1973. The high-low quartz transition up to 10 kilobars pressure. J. Geol. 81, 717–724. http://dx.doi.org/10.1086/627923.

Wallis, D., Parsons, A.J., Phillips, R.J., Searle, M.P., Ferré, E.C., 2014. Comment on "interplay of deformation and magmatism in the Pangong transpressional zone, eastern Ladakh, India: implications for remobilization of the trans-Himalayan magmatic arc and initiation of the Karakoram fault" by K. Sen, B.K. Mukherjee and A.S. Collins. J. Struct. Geol. 65, 117–119. http://dx.doi.org/10.1016/j.jsg.2014.03.008.

Wallis, D., Hansen, L.N., Britton, T.B., Wilkinson, A.J., 2016. Geometrically necessary dislocation densities in olivine obtained using high-angular resolution electron backscatter diffraction. Ultramicroscopy 168, 34–45. http://dx.doi.org/10.1016/j.ultramic.2016.06.002.

Wallis, D., Hansen, L.N., Britton, T.B., Wilkinson, A.J., 2017. Dislocation interactions in olivine revealed by HR-EBSD. J. Geophys. Res. Solid Earth. http://dx.doi.org/10.1002/2017JB014513.

Wheeler, J., Mariani, E., Piazolo, S., Prior, D.J., Trimby, P., Drury, M.R., 2009. The weighted Burgers vector: a new quantity for constraining dislocation densities and types using electron backscatter diffraction on 2D sections through crystalline materials. J. Microsc. 233, 482–494. http://dx.doi.org/10.111/j.1365-2818.2009.03136.

Wilkinson, A.J., 2001. A new method for determining small misorientation from electron back scatter diffraction patterns. Scripta Mater. 44, 2379–2385. http://dx.doi.org/10.1016/S1359-6462(01)00943-5.

Wilkinson, A.J., Randman, D., 2010. Determination of elastic strain fields and geometrically necessary dislocation distributions near nanoindents using electron backscatter diffraction. Philos. Mag. 90, 1159–1177. http://dx.doi.org/10.1080/14786430903304145.

Wilkinson, A.J., Meaden, G., Dingley, D.J., 2006. High-resolution elastic strain measurement from electron backscatter diffraction patterns: new levels of sensitivity. Ultramicroscopy 106, 307–313. http://dx.doi.org/10.1016/j.ultramic.2005.10.001.